Journal of CO2 Utilization 61 (2022) 102031

Contents lists available at ScienceDirect

Journal of CO2 Utilization

journal homepage: www.elsevier.com/locate/jcou

Thermal derived bismuth nanoparticles on nitrogen-doped carbon aerogel enable selective electrochemical production of formate from CO_2

Zhipeng Liu [a,b], Jian Zhang [a], Liang Yu [a], Hao Wang [a], Xiaoxi Huang [a,*]

[a] Hoffmann Institute of Advanced Materials, Postdoctoral Innovation Practice Base, Shenzhen Polytechnic, 7098 Liuxian Blvd, Nanshan District, Shenzhen 518055, PR China

[b] Shenzhen Institute of Advanced Technology, Chinese Academy of Sciences, Shenzhen 518055, PR China

ARTICLE INFO

Keywords:
Bismuth nanoparticles
Carbon aerogel
CO_2 reduction
Electrocatalysis

ABSTRACT

Producing formate via electrochemical carbon dioxide reduction reaction (CO_2RR) is an attractive approach to carbon neutrality but suffers from low selectivity and energy conversion efficiency. Herein, we develop an efficient CO_2RR electrocatalyst composed of Bi nanoparticles supported on N-doped carbon aerogel (Bi@NCA). Based on experimental and computational results, the carbon support serves as dual roles, one is to stabilize Bi nanoparticles by nitrogen dopants, the other function is to provide high porosity with abundant active sites to enhance CO_2 adsorbability. Because of the synergistic effect between Bi nanoparticles and N-doped carbon framework, the as-obtained Bi@NCA delivers remarkable performance with moderate overpotential, and high selectivity towards formate with Faradaic efficiency surpassing 95% in a wide potential range.

1. Introduction

The ever-growing carbon dioxide emission has become a severe problem hindering the realization of carbon neutrality. Electrochemical CO_2 reduction reaction (CO_2RR), preferably driven by renewable energies, offers an appealing route to reduce the carbon footprint and transfer CO_2 into valuable chemical feedstocks simultaneously [1–3]. Nevertheless, the CO_2RR usually suffers from low energy conversion efficiency and low selectivity as diverse products can be obtained via different mechanisms. Moreover, CO_2RR in aqueous solution is inevitably accompanied by the competing hydrogen evolution reaction [4,5]. Therefore, an efficient and selective catalyst is crucial for feasible application of electrochemical CO_2RR technology to achieve the goal of carbon neutrality [6,7].

Among the diverse products of CO_2RR, formic acid (HCOOH) and formate salts ($HCOO^-$) are relatively high-value commercial chemicals that are widely used in cleaning, feed preservation, and leather processing [8,9]. Previous reports have demonstrated that metallic catalysts based on *p*-block elements (including Pb, In, Sn and Tl) afford remarkable selectivity for formate [5,10–12]. The location of Bi is near these elements in periodic table, suggesting similar chemical properties, and it has recently attracted abundant attentions as an alternative with even higher selectivity towards formate. Moreover, the toxicity of metallic Bi is low, making this environmental benign material more suitable for industrial application [13]. However, the catalytic activity of bulk Bi crystal is usually unsatisfactory, which is hindered by limited number of catalytic active sites exposed on bulk surface as well as modest electrical conductivity compared with *d*-block metals [14–16]. On the contrary, nanosized Bi can provide more active sites and shortened electronic diffusion path. Consequently, reducing the size of metallic Bi is a feasible strategy to boost its CO_2RR performance. To control the particle size, one strategy is to use organic ligands to tune the growth of nanoparticle during synthesis, such as polyvinylpyrrolidone (PVP) and polyethylene glycol (PEG) [17,18]. However, the presence of polymer ligands on the surface can block some active sites and serve as insulating layer. These drawbacks are detrimental to electrocatalysis. Another method is to disperse nanoparticles on high surface area carbon materials via chemical reduction method to avoid the migration/aggregation of active catalysts. Typical support materials are graphene, carbon nanotube and quantum dots [19–21]. Moreover, bismuth/carbon composites can be derived from Bi-MOF precursors via annealing, during the process Bi nanoparticles and carbon supports were simultaneously generated, endowing strong interaction between each other [22–24]. However, particle aggregation is inevitable during pyrolysis process because metallic Bi has relatively low melting point (273 °C) [25], which result in shadow of active sites and diminish of specific surface area. To this

* Corresponding author.
E-mail address: xiaoxihuang@szpt.edu.cn (X. Huang).

https://doi.org/10.1016/j.jcou.2022.102031
Received 2 February 2022; Received in revised form 13 April 2022; Accepted 16 April 2022

end, it's important yet difficult to synthesize well distributed bismuth nanoparticles on carbon support via one step thermal treatment.

In terms of CO_2RR, the reaction rate is correlated with several factors including intermediate binding strength, site availability, kinetic supply of reactants and transport of products [26,27]. In this regard, carbon aerogel can be an appealing substrate to support Bi nanoparticles compared with nonporous materials: firstly, high porosity of carbon aerogel can provide substantial active sites and facilitate mass transfer; secondly, the structure of carbon aerogel can be tailored by heteroatom dopants, which can generate defective sites to anchor Bi nanoparticles and prevent agglomeration. Herein, we demonstrate a facile method to synthesize effective CO_2RR catalyst constructed by Bi nanoparticles and N-doped carbon aerogel (Bi@NCA) via in-situ pyrolysis of bismuth containing chitosan hydrogel. Due to the presence of N dopants, very small Bi nanoparticles were anchored on defective carbon nanosheets, providing abundant accessible active sites. Moreover, the high porosity of the architecture facilitates the diffusion of both CO_2 and protons. With these merits, the as-obtained Bi@NCA catalyst performs remarkably in CO_2RR with high mass activity at modest overpotential, and high Faradaic efficiency towards formate in a wide potential range.

2. Experimental section

2.1. Synthesis of Bi@NCA

A Bi precursor was firstly synthesized by grading 2.0 g bismuth nitrate pentahydrate ($Bi(NO_3)_3$•$5H_2O$) together with 0.65 g ammonium bicarbonate (NH_4HCO_3). The as-obtained Bi precursor and 0.5 g chitosan were dispersed in 20 mL of 1% acetic acid aqueous solution under stirring for 30 min to form a hydrogel. The hydrogel was freeze dried, then converted into aerogel by calcining at 800 °C for 2 h in N_2 flow with a heat rate of 5 °C·min^{-1}. Afterwards, the as-obtained aerogel was ground into powder and the sample was denoted as Bi@NCA. In addition, samples were synthesized at various calcining temperatures and the corresponding were labeled as Bi@NCA-X, where X stands for the temperature. For comparison, Bi@CA was synthesized in a similar route, but chitosan hydrogel was replaced by starch paste. A physical mixture of commercial metallic Bi powder and carbon black was prepared with ratio of Bi to C similar to that in Bi@NCA.

2.2. Characterization

The microstructure and morphology of the samples were observed by field emission scanning electron microscope (SEM, Zeiss SIGMA) and transmission electron microscope (TEM, JEOL JEM 2100 F). Powder X-ray diffraction (PXRD) patterns were obtained on a Bruker D8 Advanced X-ray diffractometer using Cu Kα radiation (λ = 0.15418 nm). X-ray photoelectron spectroscopy (XPS) was conducted on a ThermoFisher Nexsa X-Ray photoelectron spectrometer with Al Kα radiation. Raman spectra were collected on a HORIBA Scientific LabRAM HR Evolution spectrometer. The concentrations of Bi in the samples were determined using an Inductively Coupled Plasma Optical Emission Spectrometer (ICP-OES, Agilent 720ES).

2.3. Electrochemical measurements

The experiment was conducted using a three-electrode system connected to an electrochemical workstation (CHI 660E). Ag/AgCl electrode and platinum foil was utilized as reference and counter electrode, respectively. The working electrode was prepared by coating the catalysts on carbon fiber paper (see details in the Supporting Information). The electrolyte was 0.5 M $KHCO_3$ solution saturated with CO_2 (pH = 7.2), which was filled in a gas-tight two-compartment H cell separated by a proton exchange membrane. The electrolyte in cathodic compartment was stirred at a rate of 300 rpm and the CO_2 gas (10 sccm) was persistently delivered into the cathodic compartment.

2.4. Product analysis

Gas products were analyzed via gas chromatography with an interval of 20 min during the electrolysis for two hours. High purity Argon (99.999%) was utilized as the carrier gas. Hydrogen (H_2) was measured using thermal conductivity detector (TCD) and CO was measured by flame ionization detector (FID) with methanizer. The detectors were calibrated by standard gas before test. The Faradaic efficiency (FE) of each product was calculated based on the integral area of peaks in gas chromatogram according to the following equation:

$$FE = (V_i \times \text{flow rate} \times N \times F \times p)/(R \times T \times i_{total}) \times 100\%$$

where Vi is the volume concentration of H_2 or CO, N is the number of electrons required to generate corresponding gas molecule, F is the Faraday constant (96485.3 C·mol^{-1}), p = 1.013 bar, R = 8.314 J mol^{-1}·K^{-1}, T = 298.15 K and i_{total} is the total steady-state current during the constant potential test.

The liquid products were quantified by nuclear magnetic resonance (NMR) spectroscopy (JEOL JEM-ECZ400S/L1) and ion chromatography (Thermo scientific ICS-1100). After electrolysis, 300 μL of electrolyte from the cathodic cell was sampled and mixed with 300 μL D_2O containing internal standard dimethyl sulfoxide (DMSO) for NMR analysis. The ratio of the area of individual liquid product peak to that of DMSO was calculated for the quantification of the corresponding amount. The FE of liquid product was calculated using the following equation:

$$FE = (N \times F \times n_{HCOO^-})/(i_{total} \times t) \times 100\%$$

where n_{HCOO^-} is the amount of formate measured in NMR.

3. Result and discussion

3.1. Structural characterization of Bi@NCA

Chitosan hydrogel was chosen as the support material due to its robust three-dimensional networks. The Bi@NCA was synthesized from uniform hydrogel composed of chitosan and Bi precursor via thermal pyrolysis as illustrated in Fig. 1. In the process of freeze-drying, the ice crystals in the hydrogel sublimated and lead to porous aerogel [28,29]. Afterwards, chitosan aerogel was carbonized via pyrolysis to form a highly porous framework and Bi precursor was simultaneously reduced into metallic Bi. Notably, Bi precursor contains a mixture of bismuth subcarbonate and hydroxide (Fig. S1), which can decompose and release gases (CO_2, NH_3 and H_2O) during the pyrolysis process. These gases can assist to generate pores in the architecture and avoid the wrapping of Bi nanoparticles by carbon sheets.

The morphology of as-obtained Bi@NCA was inspected via scanning electron microscopy (SEM). As depicted in Fig. 1b, Bi@NCA is constructed by intertwined carbon nanosheets with abundant of porosity. The Bi spheres with the size of ~10 nm are uniformly distributed on carbon matrix. It should be noted that metallic Bi melts at low temperature and tends to agglomerate. Therefore, the formation of small Bi nanoparticles during pyrolysis process suggests a strong anchoring effect of the carbon matrix as well as the confinement of porous structure. The corresponding transmission electron microscope (TEM) image (Fig. 1c) confirms the presence of ultrasmall Bi nanoparticles on the carbon sheets, consistent with the SEM observation. These nanoparticles reveal a lattice distance of 0.33 nm (Fig. 1d), corresponding to the (012) plane of metallic Bi. In addition, a contrasty image was taken by HAADF-STEM (Fig. 1e), wherein the bright and isolated spots are ascribed to Bi nanopaticles, while the dark areas correspond to carbon substrate. Note that chitosan contains substantial amino group, which is converted into N dopants in carbon matrix [30]. Consequently, the EDS elemental mapping reveals an uniform distribution of Bi, C and N in the architecture. These aforementioned observations demonstrate that Bi@NCA is composed of Bi nanoparticles decorating on highly porous N doped

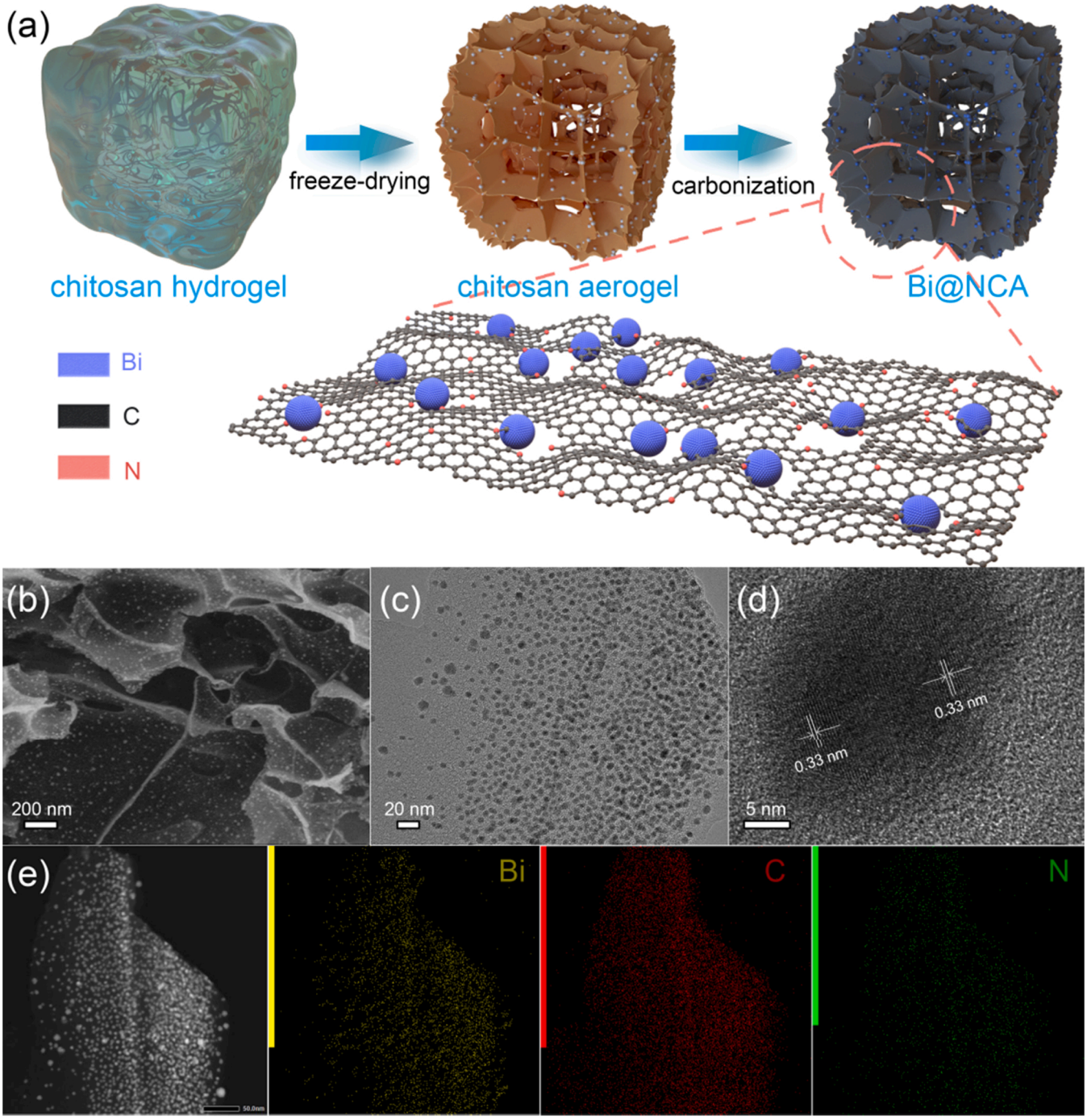

Fig. 1. (a) Schematic of the synthesis process of Bi@NCA. (b) SEM, (c) TEM, (d) HRTEM, (e) HAADF images and EDS elemental mapping of Bi@NCA.

carbon framework. It should be noted that the pyrolysis temperature is critical for the generation of ultrasmall Bi nanoparticles. The Bi precursor is converted into a mixture of metallic Bi and Bi_2O_3 at 400 °C (Fig. S2), but some microparticles are observed besides nanoparticles (Fig. S3). These microparticles shrink with the increase of temperature, resulting in Bi nanoparticles at 800 °C. At further elevated temperature of 1000 °C, Bi nanoparticles are barely observed in SEM images. In line with the SEM observation, the atomic percentage of Bi gradually decreases as the pyrolysis temperature rises according to ICP-OES results (Table S1). These phenomena are likely correlated with the volatile feature of metallic Bi:[31] Bi microparticles have weak interaction with carbon substrate and sublimate during thermal treatment, whereas the nanoparticles are more easily retained on defective sites of carbon sheets and thereby stabilized.

In order to inspect phase structure and chemical state of Bi@NCA, XRD and XPS measurements were conducted. As shown in Fig. 2a, samples obtained at 600 and 800 °C display similar patterns that are indexed to hexagonal Bi (PDF#44–1246). Peaks at 27.2°, 37.9° and 39.6° are attributed to (012), (104) and (110) planes, respectively. In contrast, no obvious signal was observed on Bi@NCA-1000 °C, implying that the majority of Bi sublimated at such high temperature. In the XPS spectrum, a dominant doublet peak raises at 164.5 and 159.2 eV (Fig. 2b), which is correlated with inevitable surface oxidation of metallic Bi [32, 33]. After removing the layer of oxides by argon plasma etching technique, the doublet peak at 162.7 and 157.4 eV becomes visible, indicating the inner metallic Bi is exposed. As mentioned above, chitosan

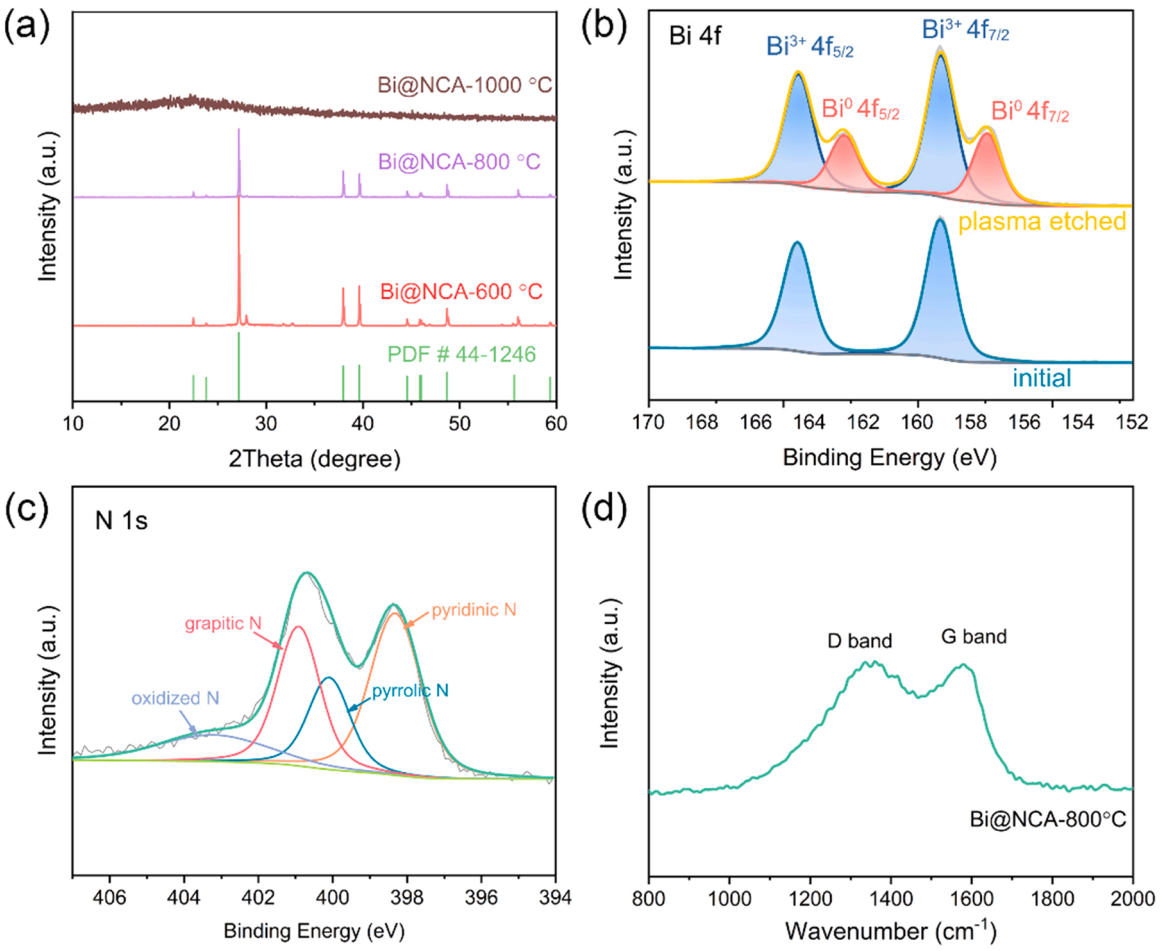

Fig. 2. (a) XRD patterns of Bi@NCA obtained at different temperatures, (b) Bi 4 f and (c) N 1 s core-level XPS spectra of Bi@NCA, (d) Raman spectra of Bi@NCA.

contains substantial nitrogen, which is in-situ doped in the carbon matrix. After deconvolution, the XPS spectrum of N 1 s of Bi@NCA exhibits peaks at 398.2, 400.3, 401.2 and 404.5 eV, assigning to pyridinic-N, pyrrolic-N, graphitic-N, and oxidized-N, respectively [29,34]. The presence of N atoms with high electronegativity can perturb the structure of carbon and lead to defective sites to stabilize metallic clusters [35–37]. For further validation, chitosan was replaced by non-nitrogen containing starch to synthesize Bi@CA. Instead of Bi nanoparticles observed on Bi@NCA, the resulting Bi on Bi@CA is in micro-sphere morphology (Fig. S4). Moreover, the density functional theory (DFT) calculations were performed to understand the origins of drastically different particle size on carbon structure derived from chitosan and starch. The optimized structures of graphene, N-doped graphene, Bi_{13} cluster supported on graphene and N-doped graphene are shown in Fig. S5. The binding energy of Bi_{13} cluster on N-doped graphene is ca. 0.2 eV lower than that on graphene, suggesting that N-doped carbon can better stabilize Bi nanoparticles. Raman measurement was also performed to estimate graphitization of carbon matrix in Bi@NCA. Two representative peaks arise at 1350 cm^{-1} for D band, and 1580 cm^{-1} for G band in carbon, respectively. The presence of intense D peak indicates a defect-rich feature of the carbon support, as this peak is generally absent or very minor in defect-free graphene [38]. The defects are likely due to the presence of heteroatom dopants derived from chitosan or the vacancy sites in carbon material generated during calcination process [39,40]. These defects endow the composite material with better structural stability by providing stronger anchoring sites for metallic Bi.

3.2. Electrochemical measurement of the CO_2RR

The CO_2RR performance of the as-obtained Bi@NCA electrocatalyst was first evaluated in 0.5 M $KHCO_3$ in gas-tight H-type cell. The LSV curves collected under N_2- and CO_2- saturated electrolyte (Fig. 3a and Fig. S6) show significant disparity. The Bi@NCA electrodes exhibit higher current and smaller overpotential under CO_2 atmosphere, indicating a higher CO_2 reduction catalytic activity. Notably, a modest potential of − 0.78 V vs. RHE was required to reach considerable current density of 10 $mA{\cdot}cm^{-2}$ and a high total current density (j_{tol}) of 61 $mA{\cdot}cm^{-2}$ was achieved at − 1.0 V vs. RHE. This value is significantly higher than that of Bi@CA and powdery Bi.

Constant potential electrolysis was performed between − 0.9 to − 1.4 V vs. RHE and the products were further analyzed by online gas chromatography (GC) and ^1H nuclear magnetic resonance (NMR) spectroscopy. As depicted in Fig. 3b, formate is the predominant product throughout the applied potential window with Faradaic efficiency (FE) around 90%. The selectivity towards formate hit the maximum of 96% at − 1.2 V vs. RHE. Besides formate, H_2 and CO was detected as minor product during electrolysis. In contrast, although formate was the major product in CO_2RR catalyzed by Bi@CA, the FEs are always lower than 90% (Fig. S7a). As a result, the corresponding partial current density (J_{HCOO^-}) normalized by geometric area is significantly lower than that in Bi@NCA (Fig. 3c). The difference is more distinct in terms of the J_{HCOO^-} calculated based on the mass loading of Bi. The partial mass current density ($mA{\cdot}mg^{-1}$) in Bi@NCA is about two times of that in Bi@CA. While in case of commercial Bi powders, the selectivity towards formate is even lower (Fig. S7b) and the J_{HCOO^-} is comparable to that in Bi@CA. In addition, the electrochemical active surface area (ECSA) was

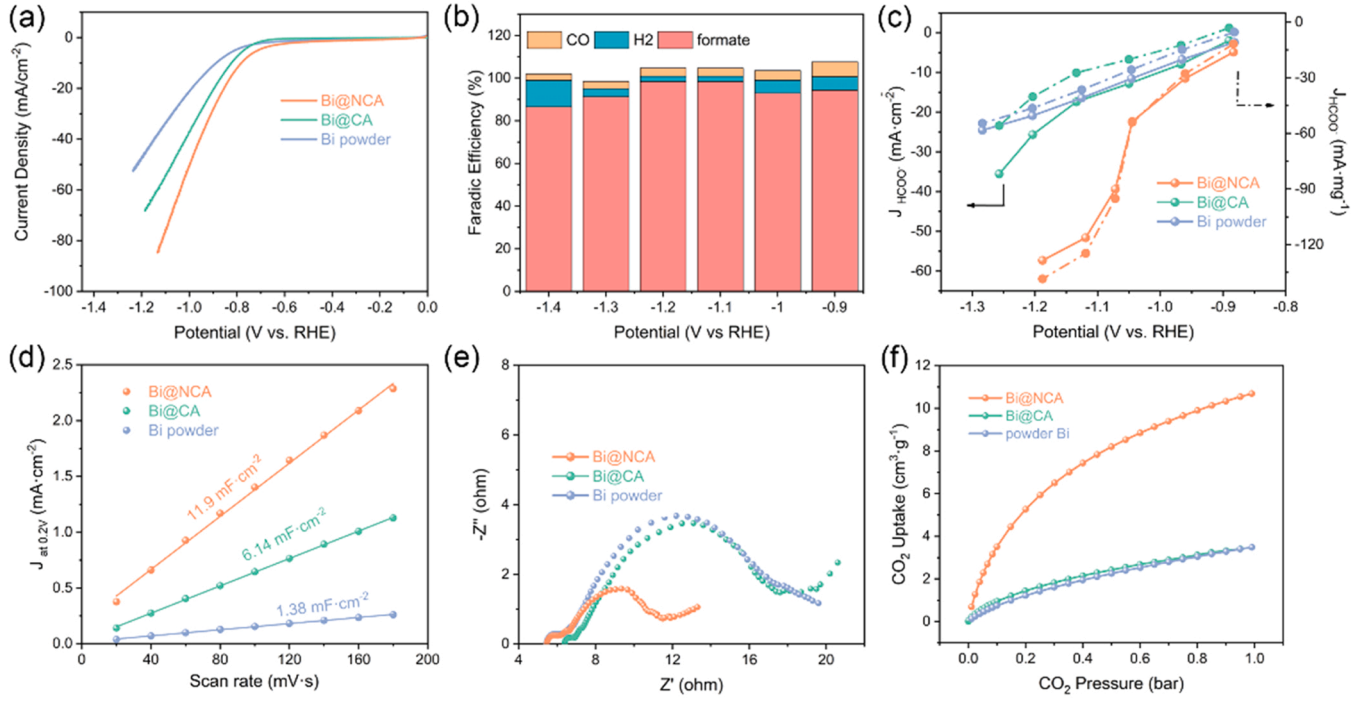

Fig. 3. Electrochemical performance of Bi@NCA, Bi@CA and Bi powder. (a) LSV curves, (b) FEs of Bi@NCA at various potential values and (c) corresponding formate partial current density normalized by geometric surface area (left axis) and mass loading of Bi (right axis). (d) Linear regressions of differences in current density ($J = J_a - J_c$) at 0.2 V plotted against the scan rates for the estimation of the electrochemical surface area. (e) Nyquist plots, (f) CO_2 adsorption isothermal curves.

estimated by measuring the double layer capacitance (Fig. S8). For comparison, Bi@NCA exhibits the highest ECSA, which is 1.9 and 8.6 times of that in Bi@CA and commercial powdery Bi, respectively (Fig. 3d). The activity normalized by ECSA is different with the trend of mass activity. This is because porous NCA support also contributes a lot to ECSA and NCA has lower intrinsic activity for CO_2RR compared with Bi. The aforementioned results demonstrate that Bi@NCA can produce formate via CO_2RR with a high activity and selectivity. In addition, tiny nanoparticles can still be observed in SEM image after the catalysis in H cell (Fig. S9). The XRD and XPS measurements confirm the presence of metallic Bi with surface oxides after the reaction process (Fig. S10).

Considering the similar compositions of Bi@NCA, Bi@CA and powdery Bi, the distinct catalytic activities are probably correlated with the different sizes of Bi, wherein Bi nanopaticles in Bi@NCA provides proliferated active sites compared with micro-sized Bi in Bi@CA. The electrochemical impedance spectra (EIS) were also measured and the resulting Nyquist diagram was plotted in Fig. 3e. Among the three samples, Bi@NCA exhibits the lowest charge transfer resistance, which reveals a facilitated electron migration at the interfaces between electrocatalyst and reactants. Such a favorable electron transfer is attributed to ultrasmall size of Bi that shortens the diffusion path. In addition to the size of Bi, the larger ECSA and lower impedance in Bi@NCA is also related with the highly porous carbon framework, which provides more available active sites and improves electronic conductivity. Furthermore, as revealed by CO_2 adsorption isotherm (Fig. 3f and Fig. S11), the porous carbon framework is beneficial in improving adsorption capability of CO_2. Notably, the accumulation of CO_2 in the vicinity of catalyst surface is prerequisite for CO_2RR. In this regard, the porous carbon substrate contributes significantly to the efficient catalytic performance of Bi@NCA as well. On the basis of aforementioned analysis, the superior catalytic performance in CO_2RR is originated from the synergistic effect between Bi nanoparticles and porous carbon framework, wherein Bi nanoparticles provide a number of active sites and enhance electron transfer, while carbon framework assists to enrich the CO_2 at surface of catalyst and accelerate electron transfer throughout the architecture.

3.3. CO_2RR in flow cell

The practical application of CO_2RR depends on an economically competitive formate production with high selectivity under large current density. However, the shortage of CO_2 in aqueous solution in H-type cell significantly hinders the CO_2 conversion rate. Therefore, the catalytic activity of Bi@NCA was further evaluated in a flow cell with an isolated gas chamber, in which CO_2 can be delivered to catalyst surface directly and react at the gas–solid-liquid triple phase boundaries (illustrated in Fig. 4a). A gas diffusion electrode was prepared by casting Bi@NCA on carbon paper to serve as the working electrode. The LSV curve (Fig. 4b) reveals that CO_2 conversion rate is significantly accelerated in the flow cell. A small potential of − 0.49 and − 1.8 V (vs. RHE) were required to achieve a current density of 10 mA·cm^{-2} and 200 mA·cm^{-2}, respectively. Moreover, the high selectivity of Bi@NCA towards formate retains at high current density. As depicted in Fig. 4c, electrolysis at high current density would not compromise selectivity (Fig. 3c and Fig. S12), for example, the $FE_{formate}$ decreases slightly from 92.3% (at 50 mA·cm^{-2}) to 88.7% at a lager current density of 250 mA·cm^{-2}, demonstrating the robust performance of Bi@NCA in flow cell reactor. To double check the results, apart from NMR analysis, ion chromatography was used to measure formate concentration in the electrolyte. At the current density of 100 mA/cm^2, the calculated $FE_{formate}$ are 92.1% and 95.6% based on NMR and IC measurements, indicating that NMR and IC techniques are comparable with each other. At last, to investigate whether the structure of Bi@NCA changes after electrolysis at high current density, the catalyst was characterized after operating at 200 mA·cm^{-2}. After 1 h of electrolysis, Bi was found to migrate to the surface of electrode, producing an array of nanosheets (Fig. S13). And we confirm that the structural evolution occurs at the initial stage of reaction and involves Bi_2CO_5 (Fig. S14) as intermediate, which is further reduced into metallic Bi. The different structural evolutions in H cell and flow cell is likely related with the difference of CO_2 concentration and operating current density.

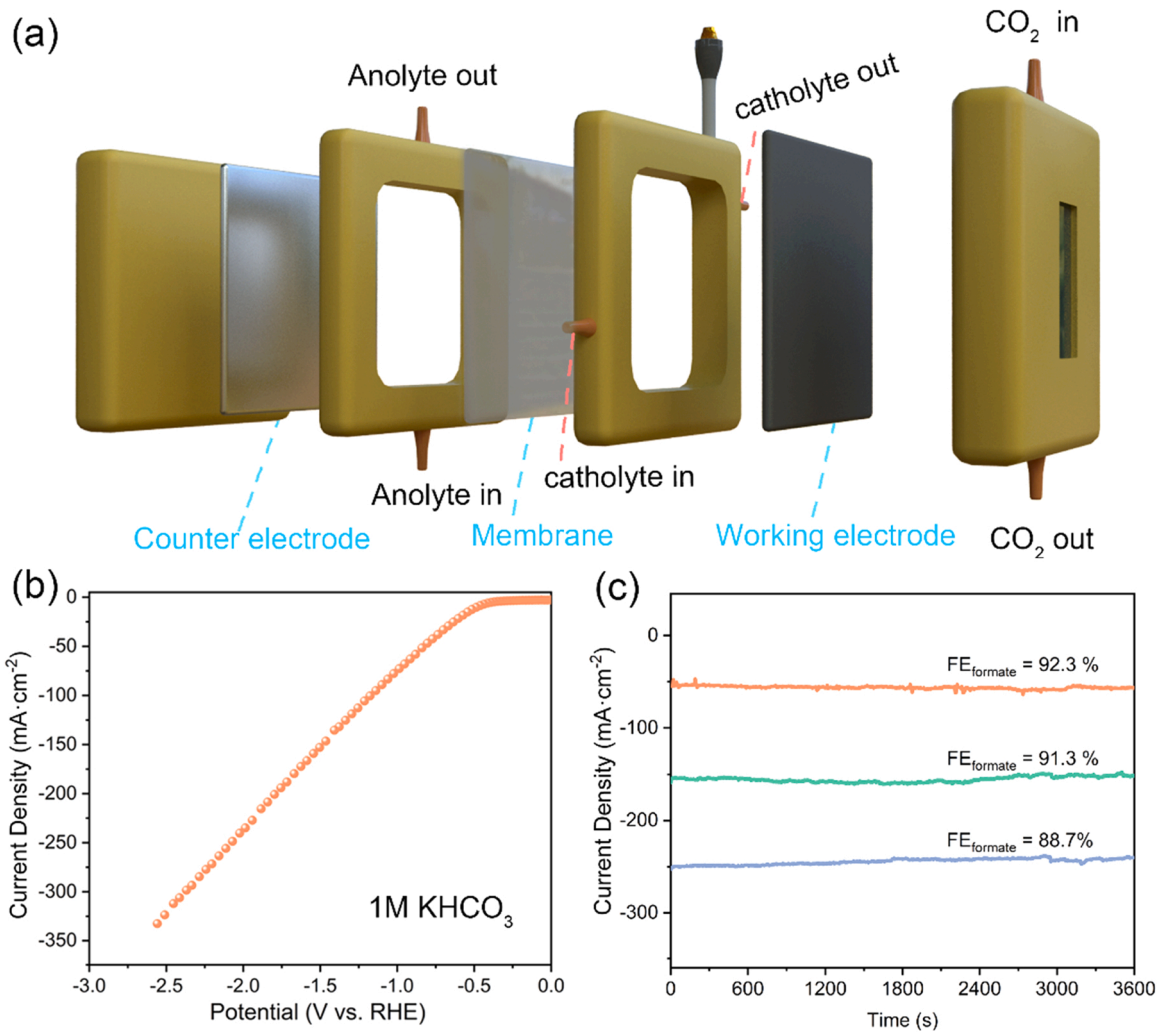

Fig. 4. Electrocatalytic CO_2RR performance of Bi@NCA in a flow cell. (a) Diagram of the flow cell, (b) LSV curve in 1 M $KHCO_3$ at a scan rate of 5 $mV{\cdot}s^{-1}$ and (c) CO_2RR in flow cell evaluated by constant potential electrolysis and corresponding $FE_{formate}$ under series of current densities.

4. Conclusion

In this work, an efficient electrocatalyst was synthesized by decorating Bi nanoparticles on N-doped carbon aerogel via facile thermal annealing method. Carbon matrix with defective structure induced by N dopants help to stabilize metallic Bi nanoparticles and prevents agglomeration. The Bi nanoparticles provide numerous active sites and facilitate electron transfer. While the carbon aerogel with high porosity enhances the adsorption of CO_2 and accessibility towards the active sites. Because of these synergistic merits, the as-obtained Bi@NCA delivers a remarkable performance with a high selectivity for formate in a wide voltage range.

CRediT authorship contribution statement

Zhipeng Liu: Conceptualization, Investigation, Methodology, Data curation, Writing – original draft. **Jian Zhang:** Methodology. **Liang Yu:** Investigation. **Hao Wang:** Resources. **Xiaoxi Huang:** Conceptualization, Supervision, Visualization, Writing – review & editing, Funding acquisition.

Declaration of Competing Interest

The authors declare that they have no known competing financial interests or personal relationships that could have appeared to influence the work reported in this paper.

Acknowledgment

This study was supported by the Scientific and Technical Innovation Council of Shenzhen (Task Book No. GXWD20201231165806004, Project No. 20200828014156001), and we also thank the support from Shenzhen Polytechnic.

Appendix A. Supporting information

Supplementary data associated with this article can be found in the online version at doi:10.1016/j.jcou.2022.102031.

References

[1] S. Nitopi, E. Bertheussen, S.B. Scott, X. Liu, A.K. Engstfeld, S. Horch, B. Seger, I.E. L. Stephens, K. Chan, C. Hahn, J.K. Norskov, T.F. Jaramillo, I. Chorkendorff, Progress and perspectives of electrochemical CO_2 reduction on copper in aqueous electrolyte, Chem. Rev. 119 (2019) 7610–7672.
[2] O.S. Bushuyev, P. De Luna, C.T. Dinh, L. Tao, G. Saur, J. van de Lagemaat, S. O. Kelley, E.H. Sargent, What should we make with CO_2 and how can we make it? Joule 2 (2018) 825–832.
[3] L. Sun, V. Reddu, A.C. Fisher, X. Wang, Electrocatalytic reduction of carbon dioxide: opportunities with heterogeneous molecular catalysts, Energy Environ. Sci. 13 (2020) 374–403.
[4] F. Pan, Y. Yang, Designing CO_2 reduction electrode materials by morphology and interface engineering, Energy Environ. Sci. 13 (2020) 2275–2309.

[5] G. Wang, J. Chen, Y. Ding, P. Cai, L. Yi, Y. Li, C. Tu, Y. Hou, Z. Wen, L. Dai, Electrocatalysis for CO_2 conversion: from fundamentals to value-added products, Chem. Soc. Rev. (2021).

[6] M.G. Kibria, J.P. Edwards, C.M. Gabardo, C.T. Dinh, A. Seifitokaldani, D. Sinton, E. H. Sargent, Electrochemical CO_2 reduction into chemical feedstocks: from mechanistic electrocatalysis models to system design, Adv. Mater. 31 (2019).

[7] X. Li, S. Wang, L. Li, X. Zu, Y. Sun, Y. Xie, Opportunity of atomically thin two-dimensional catalysts for promoting CO_2 electroreduction, Acc. Chem. Res 53 (2020) 2964–2974.

[8] I. Grigioni, L.K. Sagar, Y.C. Li, G. Lee, Y. Yan, K. Bertens, R.K. Miao, X. Wang, J. Abed, D.H. Won, F.P. García de Arquer, A.H. Ip, D. Sinton, E.H. Sargent, CO_2 electroreduction to formate at a partial current density of 930 mA cm^{-2} with InP colloidal quantum dot derived catalysts, ACS Energy Lett. 6 (2020) 79–84.

[9] C. Cao, D.D. Ma, J. Jia, Q. Xu, X.T. Wu, Q.L. Zhu, Divergent paths, same goal: a pair-electrosynthesis tactic for cost-efficient and exclusive formate production by metal-organic-framework-derived 2D electrocatalysts, Adv. Mater. 33 (2021), e2008631.

[10] X. Zheng, P. De Luna, F.P. García de Arquer, B. Zhang, N. Becknell, M.B. Ross, Y. Li, M.N. Banis, Y. Li, M. Liu, O. Voznyy, C.T. Dinh, T. Zhuang, P. Stadler, Y. Cui, X. Du, P. Yang, E.H. Sargent, Sulfur-modulated tin sites enable highly selective electrochemical reduction of CO_2 to formate, Joule 1 (2017) 794–805.

[11] M.T. Tang, H. Peng, P.S. Lamoureux, M. Bajdich, F. Abild-Pedersen, From electricity to fuels: descriptors for C1 selectivity in electrochemical CO_2 reduction, Appl. Catal. B: Environ. 279 (2020).

[12] J. Li, M. Zhu, Y.F. Han, Recent advances in electrochemical CO_2 reduction on indium-based catalysts, ChemCatChem 13 (2020) 514–531.

[13] Y. Guan, M. Liu, X. Rao, Y. Liu, J. Zhang, Electrochemical reduction of carbon dioxide (CO_2): bismuth-based electrocatalysts, J. Mater. Chem. A 9 (2021) 13770–13803.

[14] D. Wang, C. Liu, Y. Zhang, Y. Wang, Z. Wang, D. Ding, Y. Cui, X. Zhu, C. Pan, Y. Lou, F. Li, Y. Zhu, Y. Zhang, CO_2 electroreduction to formate at a partial current density up to 590 mA mg^{-1} via micrometer-scale lateral structuring of bismuth nanosheets, Small (2021), e2100602.

[15] J.H. Koh, D.H. Won, T. Eom, N.-K. Kim, K.D. Jung, H. Kim, Y.J. Hwang, B.K. Min, Facile CO_2 electro-reduction to formate via oxygen bidentate intermediate stabilized by high-index planes of bi dendrite catalyst, ACS Catal. 7 (2017) 5071–5077.

[16] S. Kim, W.J. Dong, S. Gim, W. Sohn, J.Y. Park, C.J. Yoo, H.W. Jang, J.-L. Lee, Shape-controlled bismuth nanoflakes as highly selective catalysts for electrochemical carbon dioxide reduction to formate, Nano Energy 39 (2017) 44–52.

[17] B. Avila-Bolivar, L. Garcia-Cruz, V. Montiel, J. Solla-Gullon, Electrochemical reduction of CO_2 to formate on easily prepared carbon-supported Bi nanoparticles, Molecules 24 (2019).

[18] X. Zhang, X. Hou, Q. Zhang, Y. Cai, Y. Liu, J. Qiao, Polyethylene glycol induced reconstructing Bi nanoparticle size for stabilized CO_2 electroreduction to formate, J. Catal. 365 (2018) 63–70.

[19] Y.-X. Duan, K.-H. Liu, Q. Zhang, J.-M. Yan, Q. Jiang, Efficient CO_2 reduction to HCOOH with high selectivity and energy efficiency over Bi/rGO catalyst, Small Methods 4 (2020).

[20] X. Zhang, J. Fu, Y. Liu, X.-D. Zhou, J. Qiao, Bismuth anchored on MWCNTs with controlled ultrafine nanosize enables high-efficient electrochemical reduction of carbon dioxide to formate fuel, ACS Sustain. Chem. Eng. 8 (2020) 4871–4876.

[21] Z. Chen, K. Mou, X. Wang, L. Liu, Nitrogen-doped graphene quantum dots enhance the activity of Bi_2O_3 nanosheets for electrochemical reduction of CO_2 in a wide negative potential region, Angew. Chem. Int. Ed. Engl. 57 (2018) 12790–12794.

[22] Y.-R. Wang, R.-X. Yang, Y. Chen, G.-K. Gao, Y.-J. Wang, S.-L. Li, Y.-Q. Lan, Chloroplast-like porous bismuth-based core–shell structure for high energy efficiency CO_2 electroreduction, Sci. Bull. 65 (2020) 1635–1642.

[23] J. Yang, X. Wang, Y. Qu, X. Wang, H. Huo, Q. Fan, J. Wang, L.M. Yang, Y. Wu, Bi-based metal-organic framework derived leafy bismuth nanosheets for carbon dioxide electroreduction, Adv. Energy Mater. 10 (2020).

[24] P. Deng, F. Yang, Z. Wang, S. Chen, Y. Zhou, S. Zaman, B.Y. Xia, Metal-organic framework-derived carbon nanorods encapsulating bismuth oxides for rapid and selective CO_2 electroreduction to formate, Angew. Chem. Int. Ed. Engl. 59 (2020) 10807–10813.

[25] H. Liao, J. Zhu, Y. Hou, Synthesis and electrocatalytic properties of PtBi nanoplatelets and PdBi nanowires, Nanoscale 6 (2014) 1049–1055.

[26] S. Garg, M. Li, A.Z. Weber, L. Ge, L. Li, V. Rudolph, G. Wang, T.E. Rufford, Advances and challenges in electrochemical CO_2 reduction processes: an engineering and design perspective looking beyond new catalyst materials, J. Mater. Chem. A 8 (2020) 1511–1544.

[27] A. Liu, M. Gao, X. Ren, F. Meng, Y. Yang, L. Gao, Q. Yang, T. Ma, Current progress in electrocatalytic carbon dioxide reduction to fuels on heterogeneous catalysts, J. Mater. Chem. A 8 (2020) 3541–3562.

[28] G. Sun, B. Li, J. Ran, X. Shen, H. Tong, Three-dimensional hierarchical porous carbon/graphene composites derived from graphene oxide-chitosan hydrogels for high performance supercapacitors, Electrochim. Acta 171 (2015) 13–22.

[29] H. Yu, J. Hou, R.B. Namin, Y. Ni, S. Liu, S. Yu, Y. Liu, Q. Wu, S. Nie, Pre-cryocrushing of natural carbon precursors to prepare nitrogen, sulfur co-doped porous microcellular carbon as an efficient ORR catalyst, carbon 173 (2021) 800–808.

[30] Y. He, X. Zhuang, C. Lei, L. Lei, Y. Houa, Y. Mai, X. Feng, Porous carbon nanosheets: synthetic strategies and electrochemical energy related applications, Nano Today 24 (2019) 103–109.

[31] D. Wu, X. Wang, X.-Z. Fu, J.-L. Luo, Ultrasmall Bi nanoparticles confined in carbon nanosheets as highly active and durable catalysts for CO_2 electroreduction, Appl. Catal. B: Environ. 284 (2021).

[32] K. Fan, Y. Jia, Y. Ji, P. Kuang, B. Zhu, X. Liu, J. Yu, Curved surface boosts electrochemical CO_2 reduction to formate via bismuth nanotubes in a wide potential window, ACS Catal. 10 (2019) 358–364.

[33] F. Yang, A.O. Elnabawy, R. Schimmenti, P. Song, J. Wang, Z. Peng, S. Yao, R. Deng, S. Song, Y. Lin, M. Mavrikakis, W. Xu, Bismuthene for highly efficient carbon dioxide electroreduction reaction, Nat. Commun. 11 (2020) 1088.

[34] Y. Zan, Z. Zhang, B. Zhu, M. Dou, F. Wang, Ultrathin two-dimensional phosphorus and nitrogen Co-doped carbon nanosheet as efficient oxygen reduction electrocatalyst, Carbon 174 (2021) 404–412.

[35] A. Vasileff, Y. Zheng, S.Z. Qiao, Carbon solving carbon's problems: recent progress of nanostructured carbon-based catalysts for the electrochemical reduction of CO_2, Adv. Energy Mater. 7 (2017).

[36] Y. Wang, H. Su, Y. He, L. Li, S. Zhu, H. Shen, P. Xie, X. Fu, G. Zhou, C. Feng, D. Zhao, F. Xiao, X. Zhu, Y. Zeng, M. Shao, S. Chen, G. Wu, J. Zeng, C. Wang, Advanced electrocatalysts with single-metal-atom active sites, Chem. Rev. 120 (2020) 12217–12314.

[37] Sami Ullah, Qitao Shi, Junhua Zhou, Xiaoqin Yang, M.H. Huy, Q. Ta, Nasir Mahmood Ahmad, Lei Fu, Alicja Bachmatiuk, M.H. Rümmeli, Advances and trends in chemically doped graphene, Adv. Mater. Interfaces 7 (2020), 2000999.

[38] A.C. Ferrari, J.C. Meyer, V. Scardaci, C. Casiraghi, M. Lazzeri, F. Mauri, S. Piscanec, D. Jiang, K.S. Novoselov, S. Roth, A.K. Geim, Raman spectrum of graphene and graphene layers, Phys. Rev. Lett. 97 (2006).

[39] X. Yan, Y. Jia, X. Yao, Defects on carbons for electrocatalytic oxygen reduction, Chem. Soc. Rev. 47 (2018) 7628–7658.

[40] X. Huang, L.J. Zhou, D. Voiry, M. Chhowalla, X. Zou, T. Asefa, Monodisperse mesoporous carbon nanoparticles from polymer/silica self-aggregates and their electrocatalytic activities, ACS Appl. Mater. Interfaces 8 (2016) 18891–18903.